A Backprojection-Filtration Algorithm for Nonstandard Spiral Cone-beam CT with an N-PI Window

Hengyong Yu[1], Yangbo Ye[1,2], Shiying Zhao[1], Ge Wang[1,2]

1 CT/Micro-CT Laboratory, Department of Radiology,
2 Department of Mathematics, University of Iowa,
Iowa City, Iowa, 52242, USA

Abstract: For applications in bolus-chasing CT angiography and electron-beam micro-CT, the backprojection-filtration (BPF) formula developed by Zou and Pan was recently generalized by Ye *et al.* to reconstruct images from cone-beam data collected along a rather flexible scanning locus, including a nonstandard spiral. A major implication of the generalized BPF formula is that it can be applied for n-PI-window-based reconstruction in the nonstandard spiral scanning case. In this paper, we design an n-PI-window-based BPF algorithm, and report the numerical simulation results with the 3D Shepp-Logan phantom and Defrise Disk phantom. The proposed BPF algorithm consists of three steps: cone-beam data differentiation, weighted backprojection, and inverse Hilbert filtration. Our simulated results demonstrate the feasibility and merits of the proposed algorithm.

Keywords : Cone-beam CT, nonstandard spiral scanning, PI-line, n-PI-window, backprojection-filtration (BPF).

I. Introduction

Spiral fan-beam/cone-beam computed tomography (CT) is the most important technology to reconstruct a long object. In parallel to the fast evolution of area detectors [1], spiral cone-beam reconstruction algorithms [2-22] have been under rapid development. Generally speaking, the cone-beam reconstruction algorithms may be categorized into three types: exact, approximate and iterative algorithms [2]. Ideally, the exact spiral cone-beam reconstruction algorithms are most desirable [5-20]. These exact algorithms typically utilize

the concepts of PI-lines and PI-windows, and take forms of filtered backprojection (FBP) [9-15] and backprojection-filtration (BPF) [13-20], respectively.

The original PI-line and PI-window were defined by Tam and Danielsson *et al*. [5,6] Then, these concepts and related algorithms were extended to the n-PI-window case [8,9,11]. Spiral cone-beam reconstruction based on the n-PI-window is important because it efficiently utilizes radiation dose and redundant data, and effectively reduces image noise. Proksa *et al.* proposed the first n-PI method [8] in the Grangeat framework with Radon plane triangulation. Then, they proposed a quasi-exact FBP reconstruction algorithm [9] using three sets of filter directions based on Katsevich's original formula, which is a 1-PI method [10]. Katsevich himself also formulated two FBP-type 3-PI algorithms [11]. However, all these n-PI algorithms only work with a standard helical scanning locus.

For applications in bolus-chasing CT angiography and electron-beam micro-CT, the BPF formula by Zou and Pan [16-19] was recently generalized by *Ye et al*.[15,20] for image reconstruction from cone-beam data collected along a rather flexible scanning locus, including a nonstandard spiral [14-15,20-22]. A major implication of the generalized BPF formula is that it can be applied for n-PI-window-based reconstruction in the nonstandard spiral scanning case, covering nonstandard spirals of variable pitch and/or variable radius. The result has validated Zou and Pan's claim in [16] that the BPF method can be applied to other situations such as n-PI and variable pitch helical scans [19]. In this paper, we will design an n-PI-window-based BPF algorithm. The next section defines systems and notations. The third section formulates the concepts of the n-PI-line and n-PI-window in the case of nonstandard spirals. The fourth section presents the n-PI-window-based reconstruction formula, and describes the reconstruction algorithm. The fifth section reports numerical simulation results obtained with the 3D Shepp-Logan head phantom and the Defrise disk phantom. The last section discusses a few related issues and concludes the paper.

II. Systems and Notations

Consider an object function $f(\mathbf{x})$ whose support is a cylindrical region $\mathbf{U}$. For any unit vector $\boldsymbol{\beta}$, let us define a cone-beam projection of $f(\mathbf{x})$ from a source position $\mathbf{y}(s)$ on a nonstandard 3D spiral locus $\mathbf{C}$ [20] containing $\mathbf{U}$ as

$$D_f(\mathbf{y}(s),\boldsymbol{\beta}) := \int_0^\infty f(\mathbf{y}(s)+t\boldsymbol{\beta})\, dt \tag{1}$$

$$\mathbf{C} := \left\{\mathbf{y}(s) \in \mathbb{R}^3 : y_1 = R(s)\cos(s), y_2 = R(s)\sin(s), y_3 = h(s), s \in \mathbb{R}\right\} \tag{2}$$

Note that the integral in Eq. (1) is actually taken over a finite interval, because the function $f(\mathbf{x})$ is compactly supported. When $\boldsymbol{\beta}$ points away from the support of $f(\mathbf{x})$, the integral vanishes. Without loss of generality, we assume that $h(s)$ is a monotonous increasing function depending on the X-ray source rotational angle s. For a given s, we define a local coordinate system with the three orthogonal unit directional vectors: $\mathbf{d}_1 := (-\sin(s), \cos(s), 0)$, $\mathbf{d}_2 := (0,0,1)$ and $\mathbf{d}_3 := (-\cos(s), -\sin(s), 0)$. As shown in Fig. 1, equispatial cone-beam data are measured on a planar detector array parallel to $\mathbf{d}_1$ and $\mathbf{d}_2$ at a distance $D(s)$ from $\mathbf{y}(s)$ with $D(s) = R(s) + D_c$, where D_c is a constant here but it can be readily generalized as a function of s. A detector position in the array is indexed by (u,v), which are signed distances along $\mathbf{d}_1$ and $\mathbf{d}_2$ respectively. Let $(u,v) = (0,0)$ correspond to the orthogonal projection of $\mathbf{y}(s)$ onto the detector array. If s and $D(s)$ are given, (u,v) are determined by $\boldsymbol{\beta}$. For a fixed $\mathbf{y}(s)$, $D(s)$ is constant, and cone-beam projection data can be expressed as $p(s,u,v) \equiv D_f(\mathbf{y}(s),\boldsymbol{\beta})$ with

$$u = \frac{D(s)\boldsymbol{\beta}\bullet\mathbf{d}_1}{\boldsymbol{\beta}\bullet\mathbf{d}_3} \tag{3-a}$$

$$v = \frac{D(s)\boldsymbol{\beta}\bullet\mathbf{d}_2}{\boldsymbol{\beta}\bullet\mathbf{d}_3} \tag{3-b}$$

III. Generalized N-PI-Windows and -Lines

As shown in Fig. 2, the generalized 1-PI-window [21,22] at s_0 is defined as the region in the detector plane bounded by the cone-beam projections of the upper and lower turns of

the 3D nonstandard spiral starting from the X-ray source at $\mathbf{y}(s_0)$ in the local coordinate system defined in Section II. The top and bottom boundaries of the minimum detector area Γ_{top} and Γ_{bot} are the cone-beam projections of the upper and lower spiral turns $\mathbf{y}_u(s_0,\lambda)$ and $\mathbf{y}_l(s_0,\lambda)$ respectively given by

$$\mathbf{y}_u(s_0,\lambda) = \mathbf{y}(s_0 + \pi + \lambda) \quad \text{for} \quad -\pi < \lambda < \pi, \tag{4-a}$$

$$\mathbf{y}_l(s_0,\lambda) = \mathbf{y}(s_0 - \pi + \lambda) \quad \text{for} \quad -\pi < \lambda < \pi. \tag{4-b}$$

Similar to what Ye *et al.* [21,22] and Proksa *et al.*[8,9] did, next we formulate a generalized n-PI-window at s_0. The basic idea is to extend the detector boundaries upwards and downwards simultaneously by one or more turns of the 3D nonstandard scanning spiral. The detector area is then enlarged to receive more signals from an odd number of scanning turns. In other word, we can define 3-PI-, 5-PI-windows, and so on. The upper and lower boundaries of the detector area, Γ_{top_n} and Γ_{bot_n}, are respectively the cone-beam projections of the upper and lower turns $\mathbf{y}_{u\_n}(s_0,\lambda)$ and $\mathbf{y}_{l\_n}(s_0,\lambda)$ for n being odd, which are given by

$$\mathbf{y}_{u\_n}(s_0,\lambda) = \mathbf{y}(s_0 + n\pi + \lambda) \quad \text{for} \quad -\pi < \lambda < \pi, \tag{5-a}$$

$$\mathbf{y}_{l\_n}(s_0,\lambda) = \mathbf{y}(s_0 - n\pi + \lambda) \quad \text{for} \quad -\pi < \lambda < \pi. \tag{5-b}$$

The boundary equation of Γ_{top_n} on the detector plane can be represented by

$$u = \frac{-D(s_0)R(s_0 + n\pi + \lambda)\sin(\lambda)}{R(s_0) + R(s_0 + n\pi + \lambda)\cos(\lambda)} \quad \text{for} \quad -\pi < \lambda < \pi, \tag{6-a}$$

$$v = \frac{D(s_0)\left[h(s_0 + n\pi + \lambda) - h(s_0)\right]}{R(s_0) + R(s_0 + n\pi + \lambda)\cos(\lambda)} \quad \text{for} \quad -\pi < \lambda < \pi. \tag{6-b}$$

Correspondingly, the boundary equation of Γ_{bot_n} can be represented by

$$u = \frac{-D(s_0)R(s_0 - n\pi + \lambda)\sin(\lambda)}{R(s_0) + R(s_0 - n\pi + \lambda)\cos(\lambda)} \quad \text{for} \quad -\pi < \lambda < \pi, \tag{7-a}$$

$$v = \frac{D(s_0)\left[h(s_0 - n\pi + \lambda) - h(s_0)\right]}{R(s_0) + R(s_0 - n\pi + \lambda)\cos(\lambda)} \quad \text{for} \quad -\pi < \lambda < \pi. \tag{7-b}$$

Fig. 3 illustrates a generalized 3-PI-window associated with a nonstandard spiral locus.

In the generalized n-PI-window setting, a generalized n-PI-line is defined as any line with two points $\mathbf{y}(s_b)$ and $\mathbf{y}(s_t)$ on the spiral satisfying $(n-1)\pi < s_t - s_b < (n+1)\pi$. A n-PI-segment is the segment of a n-PI-line inside the spiral. The definition of the generalized n-PI-line still makes sense because any point on the generalized n-PI-segment can be viewed from at least 180 degrees from an appropriate viewing direction, permitting accurate and reliable reconstruction [15,20].

IV. Reconstruction Algorithm

Let us define the unit vector $\boldsymbol{\beta}$ as the one pointing to $\mathbf{x} \in \mathbb{R}^3$ from $\mathbf{y}(s)$ on the nonstandard 3D spiral:

$$\boldsymbol{\beta}(\mathbf{x}, s) := \frac{\mathbf{x} - \mathbf{y}(s)}{|\mathbf{x} - \mathbf{y}(s)|} . \tag{8}$$

For a point $\mathbf{x} \in \mathbf{U}$, let us assume there exist at least one generalized n-PI-line through that point and denote the two end-points of the n-PI-segment by $\mathbf{y}\left(s_b(\mathbf{x})\right)$ and $\mathbf{y}\left(s_t(\mathbf{x})\right)$ respectively, where $s_b = s_b\left(\mathbf{x}\right)$ and $s_t = s_t\left(\mathbf{x}\right)$ are the rotation angles corresponding to these two points. Note that the uniqueness of the generalized n-PI-line is not required here. We also need a unit vector along the n-PI-line as:

$$\mathbf{e}_\pi\left(\mathbf{x}\right) := \frac{\mathbf{y}\left(s_t(\mathbf{x})\right) - \mathbf{y}\left(s_b(\mathbf{x})\right)}{\left|\mathbf{y}\left(s_t(\mathbf{x})\right) - \mathbf{y}\left(s_b(\mathbf{x})\right)\right|} \tag{9}$$

Then, let us define an integral transform kernel according to the previous results [16-20]:

$$K(\mathbf{x}, \mathbf{x}') := \frac{1}{2\pi i} \int_{\mathbb{R}^3} \operatorname{sgn}\left(\mathbf{v} \bullet \mathbf{e}_\pi(\mathbf{x})\right) e^{2\pi i \mathbf{v} \bullet (\mathbf{x} - \mathbf{x}')} d\mathbf{v} \tag{10}$$

If the 5th partial derivatives of $f(\mathbf{x})$ in the compact support $\mathbf{U}$ are absolutely integrable in $\mathbb{R}^3$, it was already proved by Ye *et al*. that [20]:

$$f(\mathbf{x}) = \int_{\mathbb{R}^3} K(\mathbf{x}, \mathbf{x}') g(\mathbf{x}') d\mathbf{x}' , \tag{11}$$

where

$$g(\mathbf{x}') := \int_{s_b(\mathbf{x})}^{s_t(\mathbf{x})} \frac{\partial}{\partial q}\Big(D_f\left(\mathbf{y}(q), \boldsymbol{\beta}(\mathbf{x}', s)\right) - D_f\left(\mathbf{y}(q), -\boldsymbol{\beta}(\mathbf{x}', s)\right)\Big)\Big|_{q=s} \frac{ds}{|\mathbf{x}' - \mathbf{y}(s)|}. \tag{12}$$

We emphasize that the BPF method as formulated by (10)-(12) can be tailored into a cone-beam algorithm for n-PI-window-based image reconstruction, which will be described as follows.

As shown in Fig. 4, for a given generalized n-PI-segment specified by s_b and s_t, a local Cartesian coordinate system can be defined based on the n-PI-line. The $x_{\pi 1}$-axis is made along the n-PI-line with its origin at the middle point of the n-PI-segment, while $x_{\pi 2}$- and $x_{\pi 3}$-axes are assigned perpendicular to the n-PI-line. In practice, only the component $x_{\pi 1}$ is used for the reconstruction according to the key relationship Eq. (13) but the $x_{\pi 2}$- and $x_{\pi 3}$ components are used for the derivation of Eq. (13). Therefore, the selection of the $x_{\pi 2}$- and $x_{\pi 3}$-axes is arbitrary. After appropriate translation and rotation transforms, any $\mathbf{x}$ in the global coordinate system can be transformed into the n-PI-line-based local coordinate system, that is, $\mathbf{x}_\pi = (x_{\pi 1}, x_{\pi 2}, x_{\pi 3})$. Following Zou and Pan's derivation steps [16], we can prove that for any fixed $\mathbf{x}_\pi$ on the n-PI-line ($x_{\pi_2} = 0$ and $x_{\pi 3} = 0$), Eq. (10) can be simplified as:

$$K(\mathbf{x}_\pi, \mathbf{x}'_\pi) = -\frac{1}{2\pi^2 (x_{\pi 1} - x'_{\pi 1})} \delta(x'_{\pi 2}) \delta(x'_{\pi 3}). \tag{13}$$

Eq. (13) shows that $K(\mathbf{x}_\pi, \mathbf{x}'_\pi)$ equals zero if $\mathbf{x}'_\pi$ is not on the n-PI-line. In other word, $K(\mathbf{x}_\pi, \mathbf{x}'_\pi)$ is a Hilbert filtering operator along the n-PI-line for a fixed point $\mathbf{x}_\pi$ on the n-PI-line.

Denote the object function and the weighted backprojection at $x_{\pi 1}$ on the n-PI-line specified by s_b and s_t as $f_\pi(x_{\pi 1}, s_b, s_t)$ and $g_\pi(x_{\pi 1}, s_b, s_t)$, respectively. Substitute (13) into (11), we have [16]

$$f_\pi(x_{\pi 1}, s_b, s_t) = -\frac{1}{2\pi^2} \int_{\mathbb{R}} \frac{dx'_{\pi 1}}{x_{\pi 1} - x'_{\pi 1}} g_\pi(x'_{\pi 1}, s_b, s_t) = -\frac{1}{2\pi} H\left\{g_\pi(x_{\pi 1}, s_b, s_t)\right\}, \tag{14}$$

where $H\{\bullet\}$ represents the Hilbert transform operator. Because $H\{H\{g\}\} = -g$ and $f_\pi(x_{\pi 1}, s_b, s_t)$ has a finite support on the n-PI-segment, we have

$$g_\pi(x_{\pi 1}, s_b, s_t) = 2\int_{x_b}^{x_t} \frac{dx'_{\pi 1}}{x_{\pi 1} - x'_{\pi 1}} f_\pi(x'_{\pi 1}, s_b, s_t), \tag{15}$$

where x_b and x_t are the minimal and maximal values of the finite support interval, respectively. Using the matrix method [14] or the method proposed by Noo *et al*. [23], we can recover $f_\pi(x_{\pi 1}, s_b, s_t)$ from the data $g_\pi(x_{\pi 1}, s_b, s_t)$ within the interval $[x_b, x_t]$.

Based on the above analysis, we have the following generalized n-PI method for image reconstruction from cone-beam data collected along a nonstandard spiral locus:

Step 1. Cone-Beam Data Differentiation:

Based on our early work [15,24], we have the following (for detail, please see the Appendix):

$$\begin{aligned} G(s,u,v) &\equiv \frac{\partial}{\partial s} D_f\left(\mathbf{y}(s), \boldsymbol{\beta}\right)\Big|_{\boldsymbol{\beta}\ fixed} = \frac{d}{ds} p(s,u,v)\,|_{\boldsymbol{\beta}\ fixed} \\ &= \left(\frac{\partial}{\partial s} + \frac{R'(s)u + u^2 + D^2(s)}{D(s)} \frac{\partial}{\partial u} + \frac{R'(s)v + uv}{D(s)} \frac{\partial}{\partial v}\right) p(s,u,v). \end{aligned} \tag{16}$$

Note that this formula was also reported in [14].

Step 2. Weighted Backprojection:

We can calculate the weighted 3D backprojection $g_\pi(x_{\pi 1}, s_b, s_t)$ of the derivatives of cone-beam data onto the n-PI-segment specified by s_b and s_t using Eqs. (12) and (3). Note that there may be a number of n-PI-lines through a given point inside the object. Hence, we may have multiple reconstructions at that point. When there are m n-PI-lines passing through the point $\mathbf{x}$, one can select any of the n-PI-line and the corresponding arc to reconstruct $f(\mathbf{x})$. This will lead to the exact reconstruction in the case of noise-free cone-beam data. In the case of noisy data, the reconstruction can be performed m times to utilize the data redundancy for noise reduction.

Step 3. Inverse Hilbert Filtering:

Finally, the object function $f_\pi(x_{\pi 1}, s_b, s_t)$ is reconstructed by solving the integral equation (15) using the matrix method [14] or the method proposed by Noo *et al*. [23].

The flowchart for this generalized BPF algorithm is drawn in Fig. 5. Since the reconstructed object function is in the n-PI-line-based local coordinate system, we need a

rebinning procedure to map the results into the global Cartesian coordinate system. The key problem is to find an n-PI-segment for a given point in the global Cartesian coordinate system, which can be done similar to what we did for the 1-PI-window-based BPF cone-beam reconstruction [13].

V. Numerical Simulation

In our numerical simulation, an elliptic spiral, whose radius and pitch have the form $R(s)=\frac{R_a R_b}{\sqrt{R_b^2\cos^2(s)+R_a^2\sin^2(s)}}$ and $h(s)=\frac{h_0 s}{2\pi}$, was used for evaluation and verification of the proposed generalized BPF algorithm, where $R_a=75\,\text{cm}$, $R_b=100\,\text{cm}$ and $h_0=10\,\text{cm}$. Both the Shepp-Logan head phantom and the Defrise Disk phantom were used after being restricted in a spherical region of 10cm radius centralized on the origin of the global Cartesian coordinate system. The distance from the detector to the z-axis (D_c) is 75cm and each detector element cover a rectangular area whose size is $0.781\times 0.781\ mm^2$. When the X-ray source was moved along a spiral turn, 1200 cone-beam projections were uniformly acquired. Totally, 3600 projections were acquired for $s\in[-3\pi,3\pi]$ for both 1-PI method and 3-PI method. The final reconstruction was done on a $256\times256\times256$ grid.

Fig. 6 shows some representative images reconstructed on n-PI-lines specified by a fixed s_b and a set of s_t. The top slices were reconstructed with a set of 1-PI-line specified by $s_b=-1.4\pi$ and $s_t\in[-0.4851\pi,-0.3149\pi]$ while the bottom slices were reconstructed with a set of 3-PI-line specified by $s_b=-1.6\pi$ and $s_t\in[1.3149\pi,1.4851\pi]$. Evidently, the phantom structures were distorted due to the n-PI-line-based local coordinate system geometry. After rebinning by interpolation, the reconstructed images were readily mapped into the global Cartesian coordinate system, as shown in Figs. 7 and 8. Figs. 6 to 8 demonstrate that the reconstructed images from generalized 3-PI-windows have the image quality visually equivalent to what reconstructed from 1-PI-windows. Compared with the original phantoms, some artifacts are observed in Figs 6 to 8. They are caused in twofold: firstly, both the 3D Shepp-Logan phantom and the Defrise Disk phantom do not satisfy the condition that their 5th partial derivatives are absolutely integrable, and this causes serious artifact near the

disconnected part of the phantoms; secondly, the numerical implementation introduces discrete error and this also results some artifacts.

To evaluate the image noise characteristics, white Gaussian noise with different normalized standard deviation (NSD) was added to the raw data synthesized from both the Shepp-Logan phantom and Defrise Disk phantom. The final reconstructed image is obtained by averaging the results from 1-PI- and 3-PI-windows for noise reduction. Without regard to the artifacts caused by discontinuity of the phantoms and discrete error, the noise of reconstructed image was measured compared to the reconstructed image from noise-free data. All the NSDs of reconstructed image were listed in Table 1 and Table 2. From Table 1 and Table 2, we get two conclusions: (a) the NSD of reconstructed noise is in proportion to the NSD of noise added to the raw projection data; (b) Noise can be reduced by averaging the results from 1-PI- and 3-PI-windows. Fig. 9 and Fig. 10 illustrate some representative averaged reconstruction slices from noisy data.

Table 1. NSDs of noise in reconstructed 3D Shepp-Logan phantom

Raw Noise(%)	1-PI-Method(%)	3-PI-Method(%)	Average(%)
0.1	0.26	0.38	0.20
0.2	0.52	0.77	0.41
0.3	0.77	1.15	0.62

Table2 NSDs of noise in reconstructed Defrise Disk phantom

Raw Noise(%)	1-PI-Method(%)	3-PI-Method(%)	Average(%)
1.0	2.58	3.83	2.06
2.0	5.16	7.67	4.11
3.0	7.74	11.50	6.40

VI. Discussions and Conclusion

We hypothesize that our n-PI-window-based algorithm may allow dynamic volumetric image reconstruction from a nonstandard spiral cone-beam scan. The earlier exact cone-beam algorithms typically take standard helical loci and explicitly assume that the object to be reconstructed does not contain time-varying structures. When these requirements are

violated in practice, serious image artifacts will be generated. The generalized BPF algorithm not only compensates for nonstandard imaging geometry but also allows a number of n-PI-lines to be used for dynamic reconstruction. Because different n-PI-segments correspond to different time windows, we have more information to recover a dynamic process in a permissible interval. Possibly, this will yield significantly better temporal resolution and temporal consistence, which are highly desirable for contrast-enhanced CT and cardiac CT, such as bolus-chasing CT angiography and electron-beam micro-CT [25].

There are several further research opportunities with the n-PI-window-based reconstruction. First, the Katsevich method for standard helical cone-beam CT may be extended into the n-PI-window and nonstandard spiral scanning geometry. This might result in a general FBP algorithm for exact image reconstruction from a nonstandard spiral cone-beam scan, which should be a counterpart of the generalized BPF algorithm presented in this paper. Then, these two algorithms can be compared for relative strengths and weaknesses to identify optimal algorithms and protocols for specific applications. We expect that the BPF algorithm would utilize the minimum amount of data, while the FBP algorithm would produce better image quality and be computationally more efficiently.

In conclusion, we have developed an n-PI-window-based BPF algorithm for nonstandard spiral scanning loci, and reported the numerical tests with the Shepp-Logan phantom and the disk phantom. Our simulation results have demonstrated that the generalized BPF method formulated by Ye *et al*. indeed produce accurate reconstructions from nonstandard spiral cone-beam scans with data contained in n-PI-windows.

Acknowledgement

This work is partially supported by a Carver Scientific Research Initiative grant and NIH/NIBIB grants EB002667 and EB004287.

Appendix: Derivation of Eq. (16)

Keeping $\boldsymbol{\beta}$ fixed and using the chain rule, the derivative of cone-beam data with respect to s can be written as

$$G(s,u,v) \equiv \frac{d}{ds} p(s,u,v)\,|_{\boldsymbol{\beta}\ \ fixed} = \frac{\partial p}{\partial s} + \frac{\partial p}{\partial u}\frac{\partial u}{\partial s} + \frac{\partial p}{\partial v}\frac{\partial v}{\partial s} \tag{A1}$$

with

$$\frac{\partial u}{\partial s} = \left(\frac{D(s)\boldsymbol{\beta}\bullet\mathbf{d}_1}{\boldsymbol{\beta}\bullet\mathbf{d}_3}\right)' = \frac{D'(s)\boldsymbol{\beta}\bullet\mathbf{d}_1 + D(s)\boldsymbol{\beta}\bullet\mathbf{d}_1'}{\boldsymbol{\beta}\bullet\mathbf{d}_3} - \frac{D(s)\boldsymbol{\beta}\bullet\mathbf{d}_1\boldsymbol{\beta}\bullet\mathbf{d}_3'}{\left(\boldsymbol{\beta}\bullet\mathbf{d}_3\right)^2} = \frac{D'(s)u + u^2 + D^2(s)}{D(s)}, \tag{A2-a}$$

$$\frac{\partial v}{\partial s} = \left(\frac{D(s)\boldsymbol{\beta}\bullet\mathbf{d}_2}{\boldsymbol{\beta}\bullet\mathbf{d}_3}\right)' = \frac{D'(s)\boldsymbol{\beta}\bullet\mathbf{d}_2 + D(s)\boldsymbol{\beta}\bullet\mathbf{d}_2'}{\boldsymbol{\beta}\bullet\mathbf{d}_3} - \frac{D(s)\boldsymbol{\beta}\bullet\mathbf{d}_2\boldsymbol{\beta}\bullet\mathbf{d}_3'}{\left(\boldsymbol{\beta}\bullet\mathbf{d}_3\right)^2} = \frac{D'(s)v + uv}{D(s)}, \tag{A2-b}$$

where Eq. (3) and the relationships $\mathbf{d}_1' = \mathbf{d}_3, \mathbf{d}_3' = -\mathbf{d}_1, \mathbf{d}_2' = 0$ have been used in the above derivation. Since $D'(s) = R'(s)$, we have

$$G(s,u,v) = \left(\frac{\partial}{\partial s} + \frac{R'(s)u + u^2 + D^2(s)}{D(s)}\frac{\partial}{\partial u} + \frac{R'(s)v + uv}{D(s)}\frac{\partial}{\partial v}\right)p(s,u,v)\,. \tag{A3}$$

References

1. M. J. Yaffe and J. A. Rowlands, "X-ray detectors for digital radiology," Physics in Medicine and Biology, 42:1-39, 1997.
2. G. Wang, C.R. Crawford, W.A. Kalender, "Multi-row-detector and cone-beam spiral/helical CT", IEEE Transactions on Medical Imaging 19(9):817-821, 2000.
3. G. Wang, TH Lin, PC Cheng, DM Shinozaki, HG Kim, "Scanning cone-beam reconstruction algorithms for x-ray microtomography", Proceedings of SPIE Vol. 1556, p. 99-112, July 1991.
4. G. Wang, T. H. Lin, P. C. Cheng and D. M. Shinozaki, "A general cone-beam reconstruction algorithm", IEEE Transaction on Medical Imaging, 12(3):486-496, 1993.
5. P.E. Danielsson, P. Edholm, and M. Seger, "Toward exact 3d-reconstruction for helical cone-beam scanning of long objects: A new detector arrangement and a new completeness

condition." In: Proceedings of the 1997 International Meeting on Fully Thre-Dimensional Image Reconstruction in Radiology and Nuclear Medicine (Pittsburgh), pp141-144. 1997.

6. K.C.Tam, "Three-dimensional computerized tomography scanning method and system for large objects with small area detectors", US Patent 5-390-112, 1995.

7. K. C. Tam, S. Samarasekera, and F. Sauer; "Exact cone-beam CT with a spiral scan"; Physics in Medicine and Biology, 43:1015–1024, 1998.

8. R. Proksa, Th. Kohler, M. Grass and J. Timmer, "The n-PI-method for helical cone-beam CT", IEEE Transactions on Medical Imaging, 19(9):848-863, 2000.

9. C. Bontus, Th. Kohler and R. Proksa, "A quasiexact reconstruction algorithm for helical CT using a 3-PI acquisition", Medical Physics, 30(9):2493-2502, 2003.

10. A. Katsevich, "Improved exact FBP algorithm for spiral CT", Adv. Appl. Math, 32:681-697, 2004.

11. A. Katsevich, "On two versions of a 3-pi algorithm for spiral CT", Physics in Medicine and Biology. 49: 2129-2143, 2004.

12. A. Katsevich, S. Basu and J. Hsieh, "Exact filtered backprojection reconstruction for dynamic pitch helical cone beam computed tomography", Physics in Medicine and Biology. 49: 3089-3103, 2004.

13. H. Yu and G. Wang, "Studies on implementation of the Katsevich algorithm for spiral cone-beam CT", Journal of X-ray Science and Technology; 12(2):97-116, 2004.

14. H. Yu, Y. Ye and G. Wang, "Katsevich-type algorithms for variable radius spiral cone-beam CT", Proceedings of SPIE, Vol 5535, p550-557, August 2004.

15. S. Zhao, H. Yu and G. Wang, "A family of analytic algorithms for cone-beam CT", Proceedings of SPIE, Vol 5535, p318-328, August 2004.

16. Y. Zou and X. Pan, "Exact image reconstruction on PI-lines in helical cone beam CT", Physics in Medicine and Biology. 49: 941-959, 2004.

17. Y. Zou and X. Pan, “Image reconstruction on PI-lines by use of filtered backprojection in helical cone-beam CT”, Physics in Medicine and Biology. 49: 2717-2731, 2004.

18. Y. Zou and X. Pan, “An extended data function and its generalized backprojection for image reconstruction in helical cone-beam CT ”, Physics in Medicine and Biology. 49: N383-N387, 2004.

19. Y. Zou, X. Pan, D. Xia and G. Wang, “Exact image reconstruction in helical cone-beam CT with a variable pitch”, Under review.

20. Y. Ye, S. Zhao, H. Yu and G. Wang, “Exact reconstruction for cone-beam scanning along nonstandard spirals and other curves”, Proceedings of SPIE, Vol 5535, p293-300, August 2004.

21. Y. Ye, J. Zhu, and G. Wang, “Minimum detection windows, PI-line existence and uniqueness for helical cone-beam scanning of variable pitch”, Medical Physics 31(3):566-572, 2004.

22. Y. Ye, J. Zhu, and G. Wang, “Geometric studies on variable radius spiral cone-beam scanning”, Medical Physics 31(6):1473-1480, 2004.

23. F. Noo, R. Clackdoyle and J.D. Pack, “A two-step Hilbert transform method for 2D image reconstruction”, Physics in Medicine and Biology. 49: 3903-3923, 2004.

24. H. Yu and G. Wang, “Feldkamp-type VOI reconstruction from super-short-scan cone-beam data”, Medical Physics, 31(6):1357-1362, 2004.

25. G. Wang, Y. Liu, Y. Ye, *et al*, “Top-level design and preliminary physical analysis for the first electron-beam micro-CT scanner”, Journal of X-Ray Science and Technology, in press.

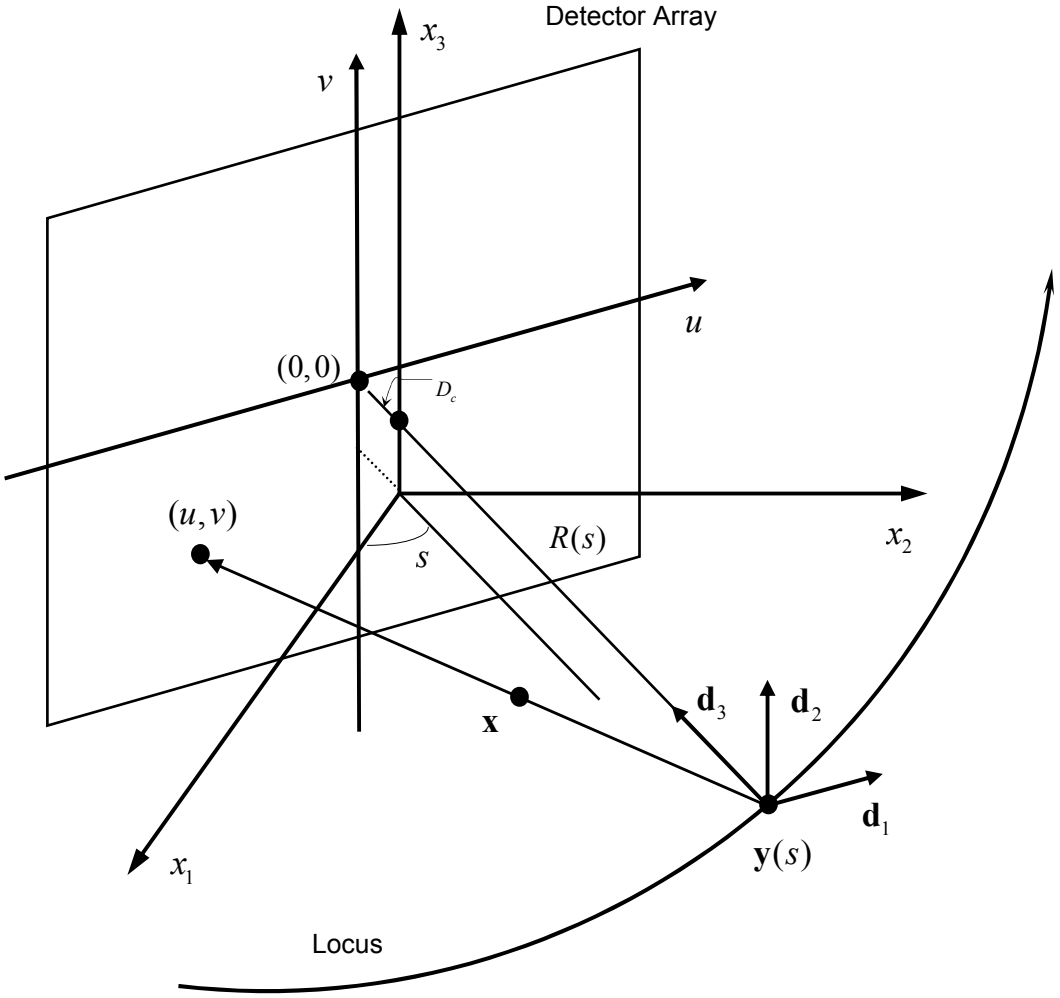

Figure 1. Local coordinate system for cone-beam projection measurement on a planar detector.

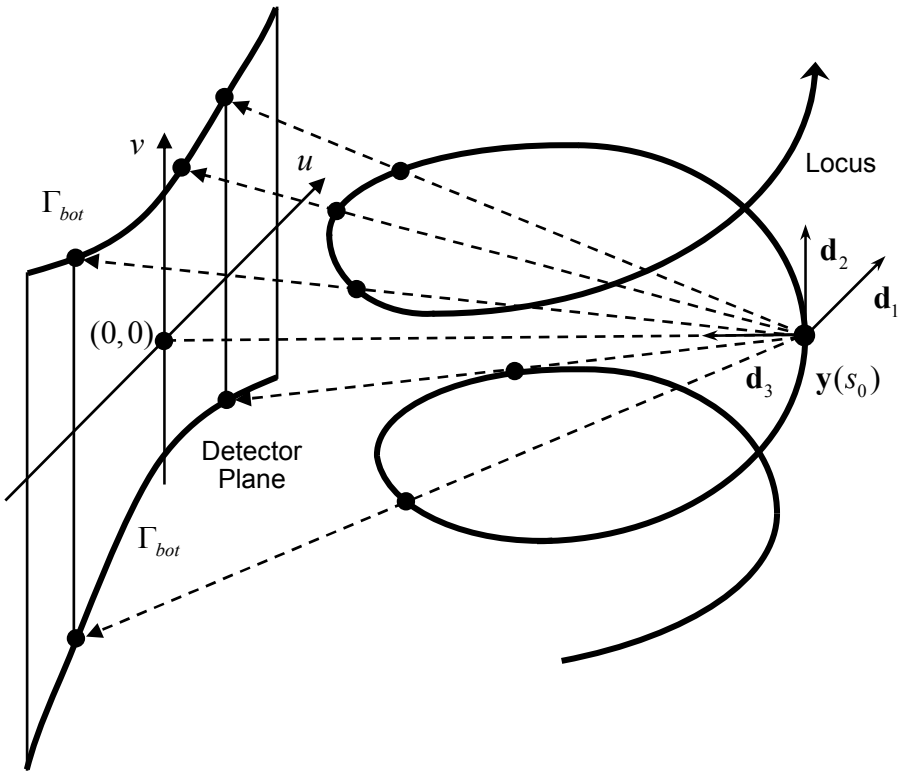

Figure 2. Generalized 1-PI-window associated with a nonstandard spiral scanning locus.

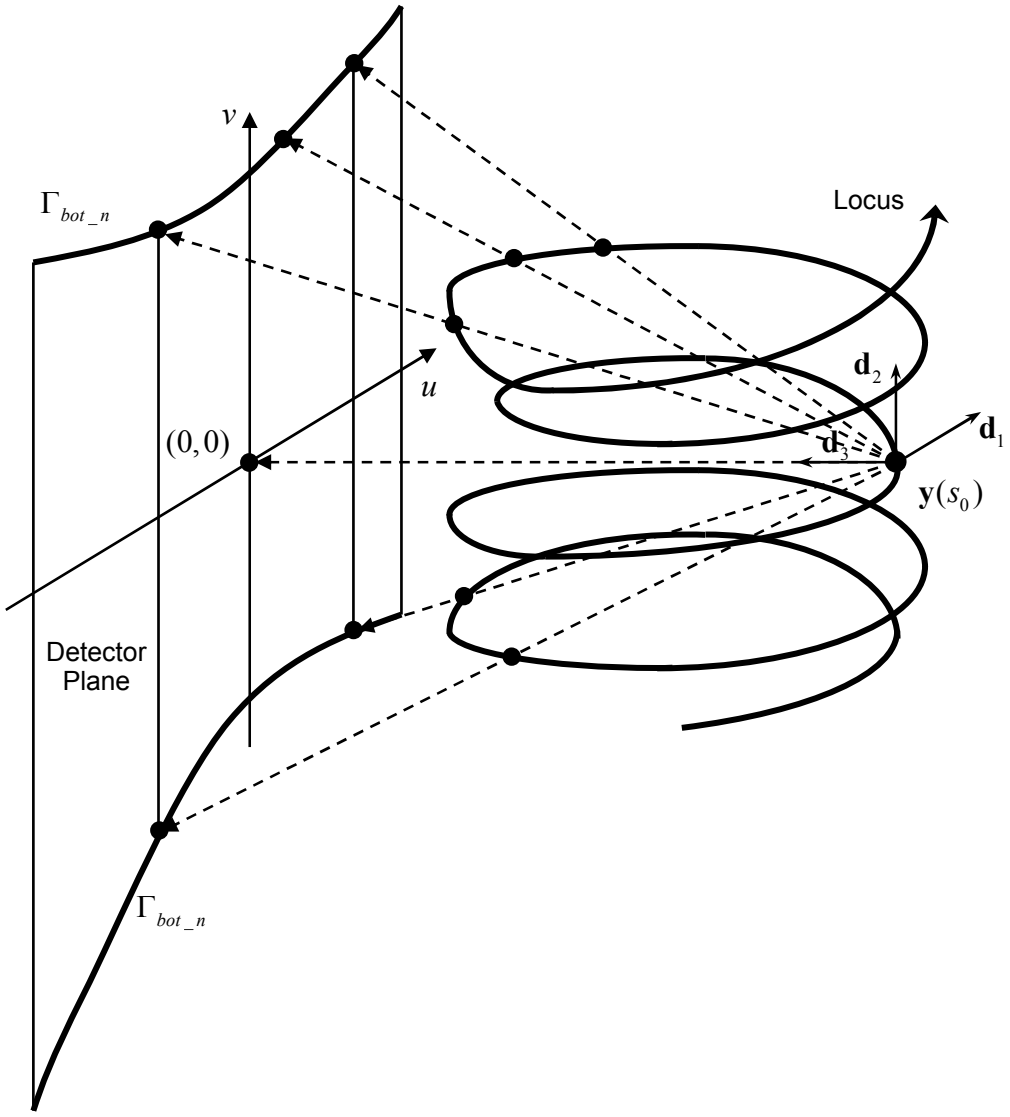

Figure 3. Generalized 3-PI-window associated with a nonstandard spiral scanning locus.

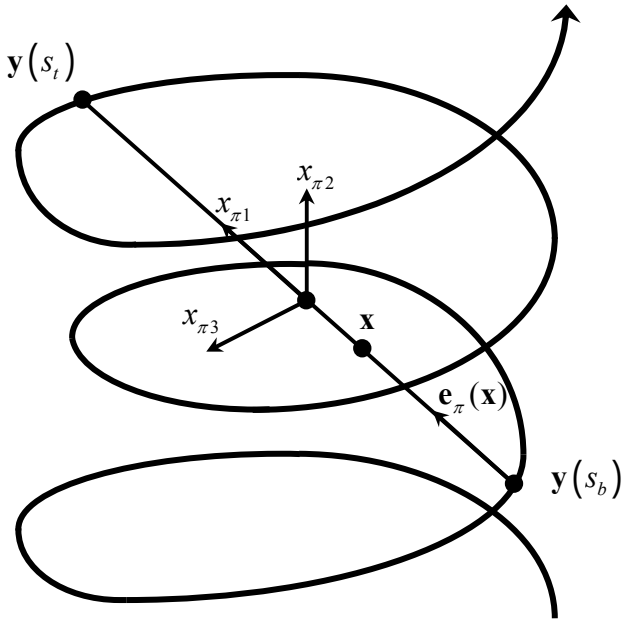

Figure 4. Local Cartesian coordinate system based on 3-PI-line.

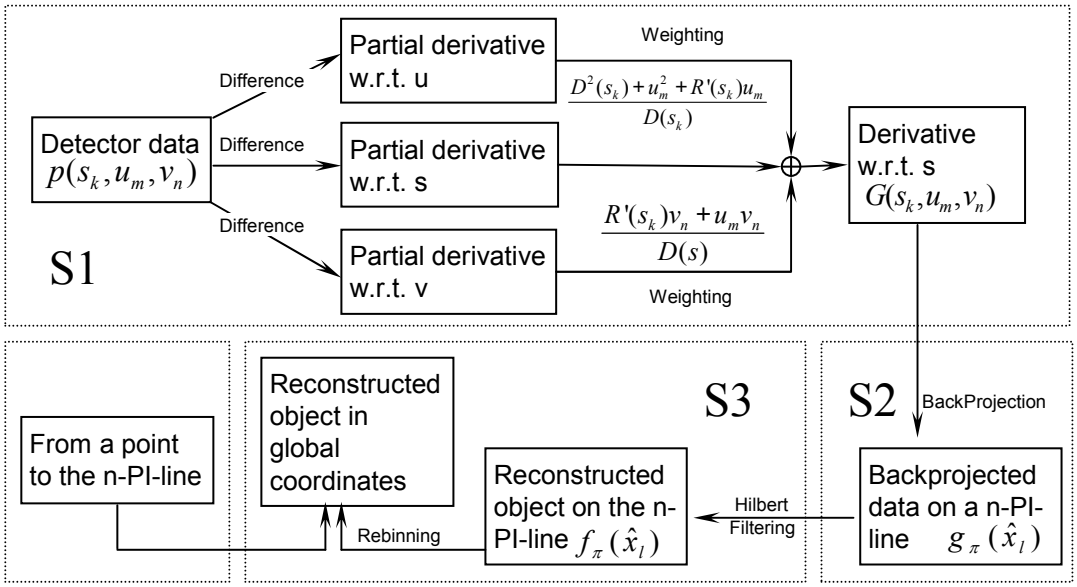

Figure5. Flowchart for the n-PI-method for nonstandard spiral cone-beam CT.

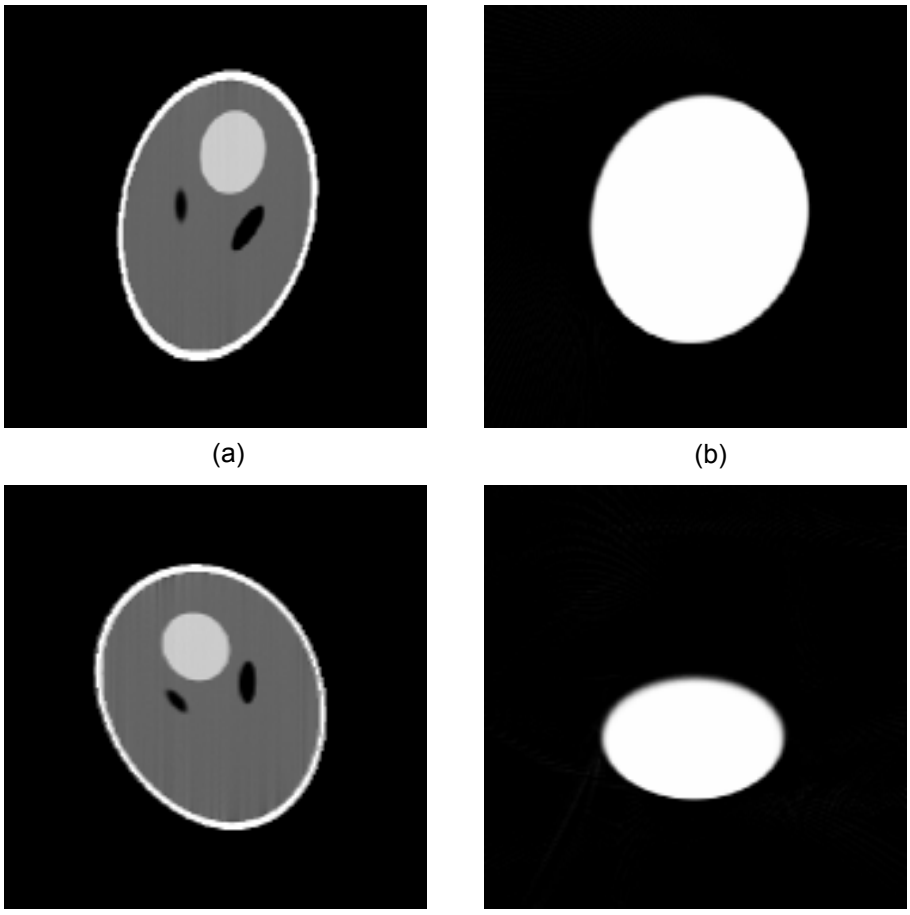

Figure 6. Reconstructed slices specified by a set of n-PI-lines. The left slices are for the Shepp-Logan head phantom with a display window [1.0,1.05] while the right slices are for the Defrise disk phantom with a display window [0,1.0]. The top slices were reconstructed from 1-PI-windows while the bottom slices were done from 3-PI-windows.

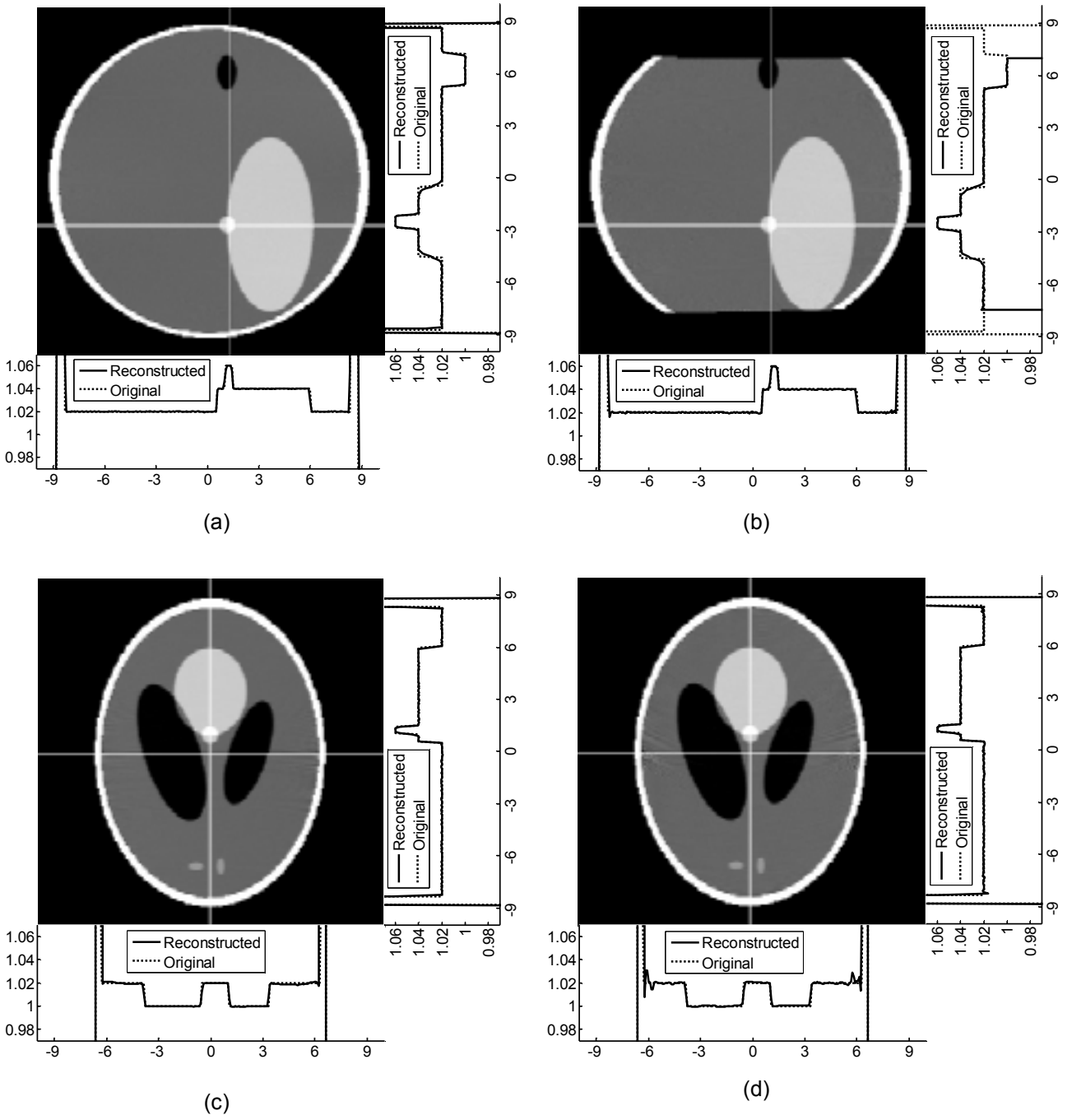

Figure 7. Reconstructed slices of the Shepp-Logan phantom in the global Cartesian coordinate system with the display window [1, 1.05]. The left slices were reconstructed from 1-PI-window data while the right slices were from 3-PI-window data. The top and bottom slices are at X=0cm and Z=-2.5cm, respectively. The two profiles along the white lines are plotted for each slice. The dotted and solid curves represent the original and reconstructed profiles.

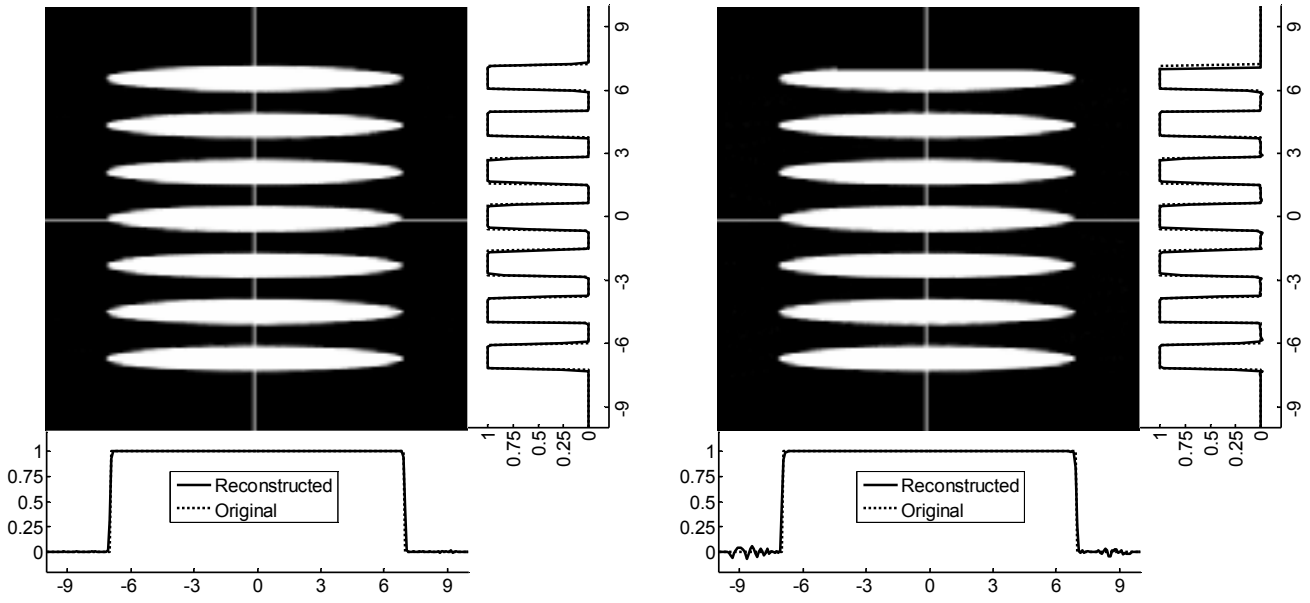

(a) (b)

Figure 8. Reconstructed slices at X=0cm of the Defrise phantom in the global Cartesian coordinate system with the display window [0, 1]. (a) was reconstructed from 1-PI-window data (b) was from 3-PI-window data. The two profiles along the white lines are plotted for each slice. The dotted and solid curves represent the original and reconstructed profiles.

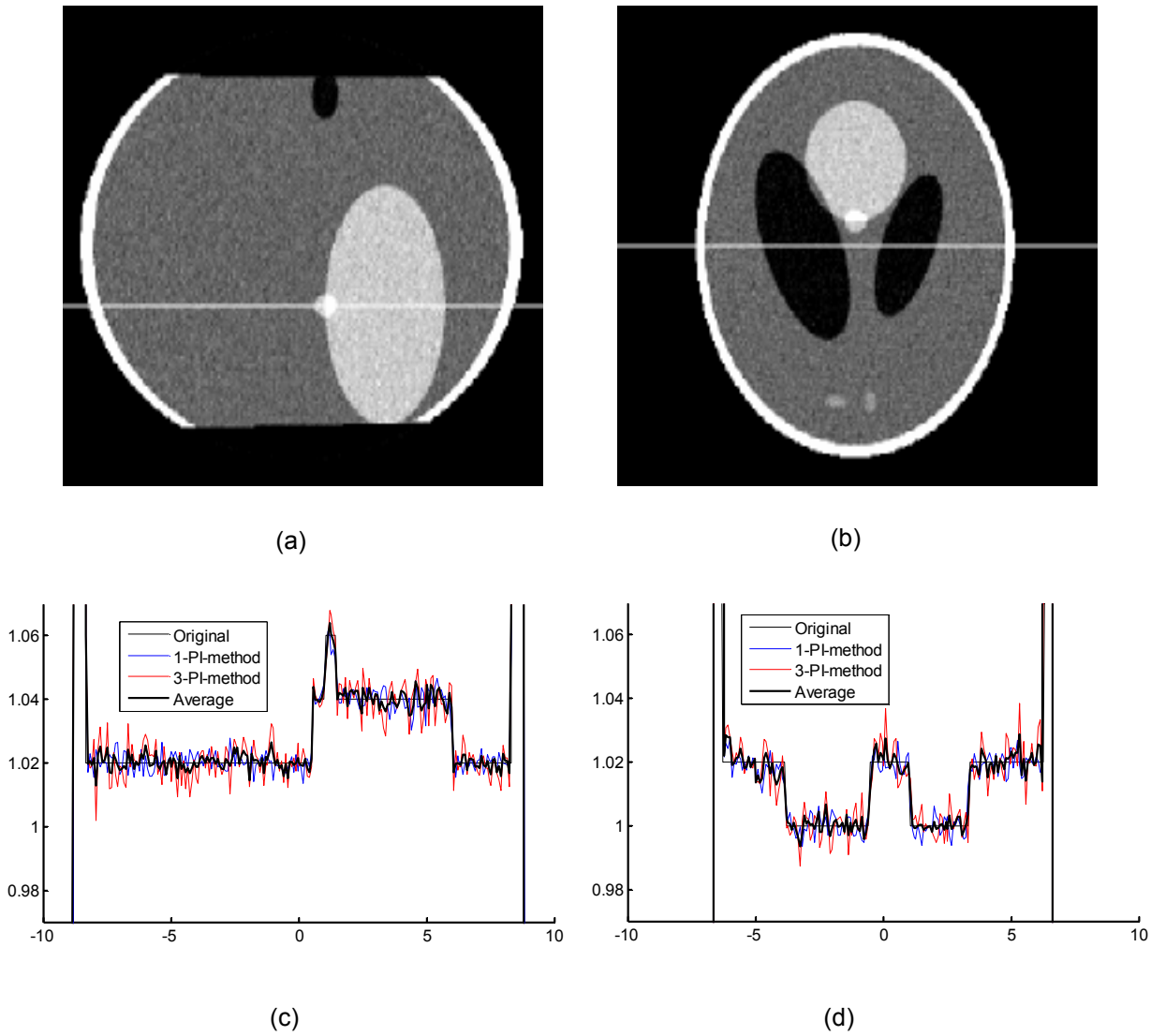

Figure 9. Reconstructed slices of the 3D Shepp-Logan phantom from 0.1% noisy data in the global Cartesian coordinate system with the display window [1,1.05]. (a) and (b) are slices at X=0cm and Z=-2.5cm, respectively. (c) and (d) are profiles along the white lines in (a) and (b), respectively.

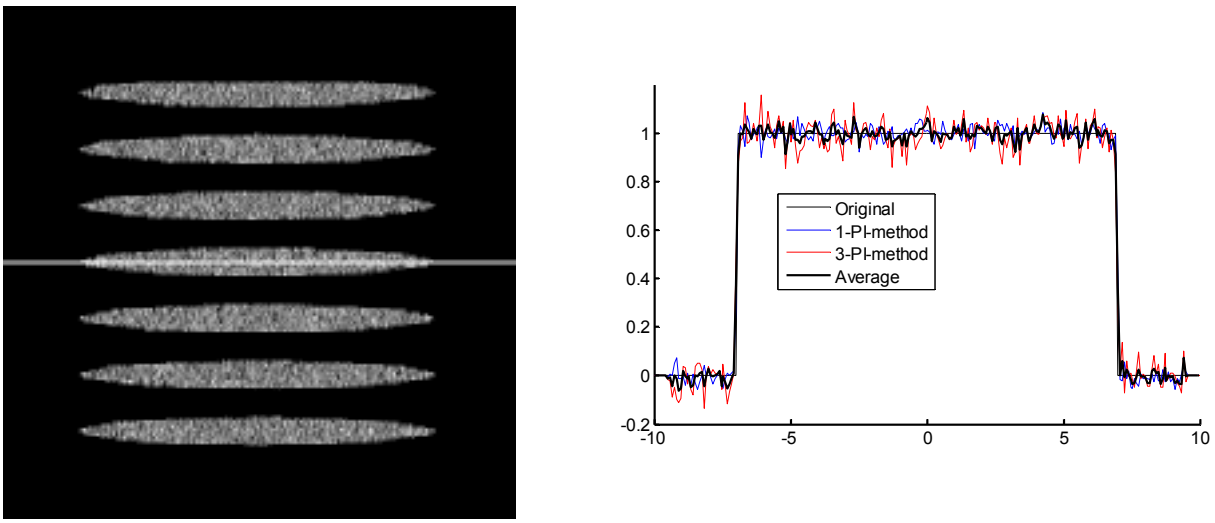

(a) (b)

Figure 10. Reconstructed slice at X=0cm of the Defrise Disk phantom from 1.0% noisy data in the global Cartesian coordinate system with the display window [0.9,1.1]. (a) is the image of the slice and (b) is the profile along the white line in (a).